IEEE Access
Multidisciplinary : Rapid Review : Open Access Journal

Received June 18, 2020, accepted July 4, 2020, date of publication July 27, 2020, date of current version August 12, 2020.

Digital Object Identifier 10.1109/ACCESS.2020.3012011

A 3D Non-Stationary GBSM for Vehicular Visible Light Communication MISO Channels

AHMED AL-KINANI[1], CHENG-XIANG WANG[2,3,4], (Fellow, IEEE), QIUMING ZHU[5], (Member, IEEE), YU FU[4], EL-HADI M. AGGOUNE[6], (Life Senior Member, IEEE), AHMED TALIB[7], AND NIDAA A. AL-HASAANI[7]

[1]Cellular Asset Management Services Ltd., Surrey TW20 8HE, U.K.
[2]National Mobile Communications Research Laboratory, School of Information Science and Engineering, Southeast University, Nanjing 210096, China
[3]Purple Mountain Laboratories, Nanjing 211111, China
[4]School of Engineering and Physical Sciences, Institute of Sensors, Signals, and Systems, Heriot-Watt University, Edinburgh EH14 4AS, U.K.
[5]College of Electronic and Information Engineering, Nanjing University of Aeronautics and Astronautics, Nanjing 211106, China
[6]Sensor Networks and Cellular Systems Research Center, University of Tabuk, Tabuk 71491, Saudi Arabia
[7]Informatics and Telecommunication Public Company (ITPC), Ministry of Communications of Iraq, Baghdad 10013, Iraq

Corresponding author: Cheng-Xiang Wang (chxwang@seu.edu.cn)

This work was supported in part by the National Key Research and Development Program of China under Grant 2018YFB1801101; in part by the National Natural Science Foundation of China (NSFC) under Grant 61960206006 and Grant 61871035; in part by the Frontiers Science Center for Mobile Information Communication and Security; in part by the High Level Innovation and Entrepreneurial Research Team Program in Jiangsu; in part by the High Level Innovation and Entrepreneurial Talent Introduction Program in Jiangsu; in part by the Research Fund of National Mobile Communications Research Laboratory; in part by the Southeast University, under Grant 2020B01; in part by the Fundamental Research Funds for the Central Universities under Grant 2242020R30001; in part by the Huawei Cooperation Project; in part by the EU H2020 RISE TESTBED2 Project under Grant 872172; in part by the Ministry of Communications of Iraq under Grant 821978; and in part by the Sensor Networks and Cellular Systems (SNCS) Research Center, University of Tabuk, under Grant 1440-503.

ABSTRACT The potential of using visible light communication (VLC) technologies for vehicular communication networks has recently attracted much attention. The underlying VLC channels, as a foundation for the proper design and optimization of vehicular VLC communication systems, have not yet been sufficiently investigated. Vehicular VLC link impairments can have a significant impact on the system performance and capacity. Such impairments include the optical wireless channel distortion and background noise. This paper proposes a novel three-dimensional (3D) regular-shaped geometry-based stochastic model (RS-GBSM) for vehicular VLC multiple-input single-output (MISO) channels. The proposed 3D RS-GBSM combines a two-sphere model and an elliptic-cylinder model. Both the line-of-sight (LoS) and single-bounced (SB) components are considered. The proposed model jointly considers the azimuth and elevation angles by using von-Mises-Fisher (VMF) distribution. Based on the proposed model, the relationship between the communication range and the received optical power is analyzed and validated by simulations. The impact of the elevation angle in the 3D model on the received optical power is investigated by comparing with the received optical power of the corresponding two-dimensional (2D) model. Furthermore, the background noise is also modeled to evaluate the system's signal-to-noise ratio (SNR).

INDEX TERMS 3D RS-GBSM, non-stationarity, SNR, vehicular visible light communications, statistical properties.

I. INTRODUCTION

The annual global road crash statistics revealed that road accidents are the direct cause of death for about 1.3 million people every year. Globally, it is estimated to cost USD 518 billion [1]. Therefore, researchers have been focusing on vehicular communication technologies towards accident-free traffic environment. Vehicular communication networks facilitate information sharing between cars and with the surrounding environments. Such information is quite useful for facilitating road safety. During the past few years, considerable research endeavors have been attempted towards the

The associate editor coordinating the review of this manuscript and approving it for publication was S. Sofana Reka.

adaptation of vehicle-to-vehicle (V2V), vehicle-to-roadside (V2R), and roadside-to-vehicle (R2V) communications to intelligent transportation systems (ITS). However, ongoing research efforts are focusing on developing the existing technologies toward vehicle-to-everything (V2X) communications. V2X strives towards data sharing between vehicles and homes, pedestrians, grids, devices or other entities that can influence the vehicle.

Recently, vehicular ad-hoc networks (VANET) gained enormous attention and became a key part of ITS to reinforce safety on the roads, increase traffic efficiency, and ensure the safety and comfort of drivers, travelers, and passersby [2]. VANET use dedicated short range communications (DSRC) and wireless access in vehicular environments (WAVE) standards for secure and fast vehicular communications. The implementation of DSCR/WAVE technologies requires new hardware to be added. However, supporting the existing infrastructures and vehicles with new hardware will add extra costs and increase power consumption. On the other hand, visible light communications (VLCs) have attracted ever-growing attention as a complementary technology to radio frequency (RF) based wireless communications for indoor and outdoor wireless environments [3]. This brought the idea of exploiting state-of-the-art VLC technique to be integrated with vehicular communications to propose vehicular VLC (VVLC) [4]. VLC systems take an advantage of commercially available incoherent light-emitting diode (LED) to serve as an optical transmitter (Tx). On the other hand, the optical receiver (Rx) employs a highly sensitive photodiode (PD) or a camera receiver [5].

In order to get optimum VLC system design, explicit knowledge for the optical wireless propagation channel is vital to understand the channel impact on system performance. Considerable research efforts have been carried out related to VVLC channel modeling in terms of V2R scenarios such as traffic light control at intersections [6]–[8]. But only the line-of-sight (LoS) channel was taken into account for specific scenarios of applications. These models are deterministic and depend solely on the Tx-Rx distance. Whilst in reality, the received signal consists of LoS and non-LoS (NLoS) components. NLoS components result from reflections off the surrounding obstacles. Furthermore, ray-tracing based channel models for V2V and V2R VVLC channels were proposed in [9], [10]. Ray-tracing channel modeling is a deterministic and reliable but time-consuming approach and cannot be extended to a broad range of scenarios [11]. In [12] the authors considered measurements campaign in [13], where both LoS and NLoS links are considered using a geometry-based road-surface reflection channel model. However, the model takes into account the reflections off the blacktop while ignoring other reflections from the surrounding vehicles. As an attempt to fill the above research gap, we previously proposed a two-dimensional (2D) non-stationary regular-shaped geometry-based stochastic model (RS-GBSM) for VVLC single-input single-output (SISO) channels [14]. The proposed model considers the LoS and NLoS links and takes into account the surrounding vehicles and the stationary roadside environments. In order to develop the existing 2D RS-GBSM, we propose a three-dimensional (3D) RS-GBSM for the sake of more accurate characterization of VVLC channel models. Due to their reasonable complexity and mathematical traceability, 3D RS-GBSMs have been utilized to investigate channel characteristics of conventional RF-based vehicular channels, as reported in [15]–[17]. However, to the best of the authors′ knowledge, this work presents the first ever efforts to investigate 3D RS-GBSM VVLC channels.

To summarize, the main contributions and novelties of the paper are highlighted as follows:

1) A 3D RS-GBSM is proposed for VVLC multiple-input single-output (MISO) channels considering the surrounding moving vehicles and stationary roadside environment.
2) We utilize the proposed 3D RS-GBSM to drive and investigate VVLC channels' characteristics such as received optical power and signal-to-noise ratio (SNR).
3) The main differences between conventional RF-based vehicular and VVLC systems are addressed.
4) The proposed 3D RS-GBSM is compared with the existing 2D RS-GBSM.
5) We also investigate the impacts of von-Mises-Fisher (VMF) distribution parameters and elevation angle on VVLC channel characteristics.

The rest of this paper is structured as follows. Section II describes the proposed VVLC MISO system model including the headlamp (Tx) and optical receiver (Rx) models. In Section III, the description of the proposed 3D RS-GBSM and the derivations of channel parameters are presented. Section IV presents the investigated VVLC channel characteristics using von Mises-Fisher (VMF) distribution. Numerical and simulation results are shown and analyzed in Section V. Finally, conclusions are made in Section VI.

II. VVLC MISO SYSTEM MODEL

A. VVLC SYSTEM MODEL

Compared with classical RF-based vehicular communication systems, VVLC is classified as small spatial scale (SSS) communication scenario since the Tx-Rx distance is between 30 and 300 m [18]. Unlike conventional RF V2V communication systems, VLC employ intensity modulation (IM) technique since incoherent LEDs cannot directly be phase or frequency modulated [19]. For signal recovery, direct detection (DD) technique is used. Table 1 presents the key differences between the conventional RF (DSRC) vehicular systems and VVLC systems.

New cars have front, tail, and wing mirrors indicator LED lights that can be used as Txs. While a PD or a camera-based receiver can serve as a Rx. Fig. 1 shows a typical geometrical description of the proposed VVLC scenario with LoS and single-bounced (SB) rays. In this paper, only SB rays are considered since the powers of double-bounced (DB) rays are significantly low and can be disregarded especially for outdoor VLC applications as we have demonstrated in our previous work [14].

In general, to model VVLC channels, road traffic and light propagation need to be modeled considering Tx radiation pattern and Rx aperture size [20]. In terms of road traffic modeling, Fig. 1 illustrates a VVLC system model utilized in urban canyon environments.

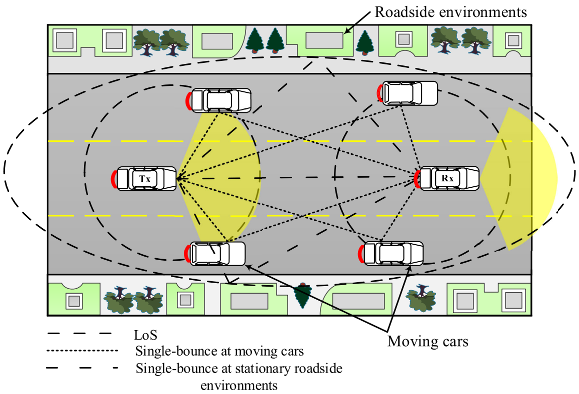

FIGURE 1. The proposed VVLC MISO system model.

We assume that there are effective scatterers positioned on 3D ordinary shapes, namely, two spheres and an elliptic-cylinder. The two-sphere model proposes the Tx-sphere and Rx-sphere which are shaping the effective scatterers around the Tx and Rx, respectively. These scatterers represent adjacent moving vehicles. While the elliptic-cylinder model is proposed to model the stationary roadside environments such as architectures, road signages, parked vehicles, and trees. An effective scatterer can involve several closely located physical scatterers that are unresolvable in the delay domain [17]. On the other hand, regarding light propagation from the Tx to the Rx, we assume that both the left-side headlight (LSH) and right-side headlight (RSH) have identical output light distribution. Consequently, the received power is composed of LoS and NLoS components. It is worth mentioning that the NLoS components are due to the reflection of LSH and RSH lights off both two-sphere and elliptic-cylinder models. Since there are two headlights at the Tx vehicle and a specific one Rx at the target vehicle, the proposed system is assumed as a MISO system model.

In order to introduce the problem of MISO channel modeling, we assume that the VVLC MISO system consists of LSH and RSH headlights with transmit powers of $P_{\mathrm{Tx-LSH}}$ and $P_{\mathrm{Tx-RSH}}$, respectively. While at the receiver side, a non-imaging P-type/Intrinsic/N-type (PIN) PD is considered. For optical wireless communications (OWC), channel effect is characterized by its impulse response $h(t)$, which is also indicated as channel impulse response (CIR) [21]. Optical CIR $h(t)$ expresses the optical power loss and hence plays a significant role to analyze channel effect on VVLC system performance. With regard to optical channels, the direct current (DC) channel gain $H(0)$ for an optical receiver is given as [22]

$$H(0) = \int_0^{\infty} h(t)dt. \tag{1}$$

DC channel gain $H(0)$ is used to characterize the losses of the optical channels.

Since each Tx will be connected with the Rx through transmission links (sub-channels), therefore, the detailed CIR of the LSH and RSH can be expressed as

$$h(t)_{\mathrm{L}} = h_{\mathrm{L}}^{\mathrm{LoS}}(t) + \sum_{n=1}^{N} h_{\mathrm{L}}^{i,j}(t) + \sum_{n=1}^{N} h_{\mathrm{L}}^{i,j}(t) + \sum_{n=1}^{N} h_{\mathrm{L}}^{i,j}(t) \tag{2}$$

and

$$h(t)_{\mathrm{R}} = h_{\mathrm{R}}^{\mathrm{LoS}}(t) + \sum_{n=1}^{N} h_{\mathrm{R}}^{i,j}(t) + \sum_{n=1}^{N} h_{\mathrm{R}}^{i,j}(t) + \sum_{n=1}^{N} h_{\mathrm{R}}^{i,j}(t). \tag{3}$$

Due to pages limit, L/R denotes LSH/RSH throughout this paper. Here, $i = 1, 2$ means we consider the contributions from both left side and right side surroundings for each headlight, namely, $i = 1$, for the left side surroundings, while $i = 2$ for the right side surroundings. On the other hand, $j = 1, 2, 3$ denotes there are three components for SB rays, which arrive from the Tx-sphere, the Rx-sphere, and the elliptic-cylinder models, respectively.

The total received power for the proposed MISO VVLC system is generally defined as

$$P_{\mathrm{Rx}} = H(0)_{\mathrm{LSH}}\, P_{\mathrm{Tx-LSH}} + H(0)_{\mathrm{RSH}}\, P_{\mathrm{Tx-RSH}}. \tag{4}$$

Here, $H(0)_{\mathrm{LSH}}$ and $H(0)_{\mathrm{RSH}}$ represent the DC channel gains of the left headlight and right headlight, respectively. If we assume that both headlights are transmitting the same power, Eq.(4) can be rewritten as

$$P_{\mathrm{Rx}} = P_{\mathrm{Tx}}\left\{H(0)_{\mathrm{LSH}} + H(0)_{\mathrm{RSH}}\right\}. \tag{5}$$

In this regards, Eq.(5) represents the most general equation for describing the received optical power of the proposed system model.

B. HEADLAMP MODEL

According to the final report from the European Commission, the advanced headlights must be designed to maximize clarity of the roadway whilst minimizing the glare towards oncoming vehicles [23]. Therefore, the pattern of light produced by a headlamp is of vital importance in VVLC. Headlamps can produce high-beam pattern for long-distance visibility on roads with no oncoming car and low-beam pattern which provides maximum forward and lateral illumination. In this work, we consider low-beam headlight since our system model has been proposed in a typical urban canyon environment. Prior to introducing headlights' radiation pattern, it is important to introduce the unit of measurement of light, which is used to measure lighting level. In terms of surface information, the total luminous flux falling on a unit area of a surface is termed illuminance (E) or illumination. Illuminance unit of measurement is lumen per square meter

TABLE 1. Comparison of VVLCs and RF (DSRC) technologies.

	VVLC	RF (DSRC)
Communication Scenario	Mainly (LoS)	LoS & NLoS
Distance	SSS	SSS, MSS, LSS
Cost	Low	High
New Hardware Required	No	Yes
Complexity	Low	High
Positioning Precision	High (cm-level)	Low
Interference	Optical (High) Electrical (Low)	Electrical (High)
Environment-friendly	Yes	No
Data Rate	hundreds of Mbps	27 Mbps
Carrier frequency	380–780 THz	5.85–5.925 GHz
License	Free	Required
Mobility	Low-Medium	High
Security	High	Low
SSS (Tx-Rx distance < 300 m); MSS: Moderate spatial scale (1 km>Tx-Rx distance > 300 m); LSS: large spatial scale (Tx-Rx distance > 1 km) [18]		

and commonly called lux (lx). The illuminance E that can be captured at a specific Rx located at a specific distance of interest can be expressed as [24]

$$E = \frac{I(\alpha_T, \beta_T)\cos(\beta_R)}{d^2}. \quad (6)$$

Here, $I(\alpha_T, \beta_T)$ is the luminous intensity in unit of candela (cd), α_T and β_T are the azimuth and elevation angles of Tx radiation pattern, respectively. Tx-Rx distance denoted as d, while β_R is the angle between the light-receiving surface normal and the light incident direction. For instance, the illuminance pattern of a headlamp equipped with a Xenon lamp is presented in Fig. 2. This diagram is called an Isolux diagram where lines indicate illuminance E levels in steps. In this example, the illuminance reaches a maximum as 100 lx at the front of the car and minimum of 1 lx at the outer line. However, such illuminance patterns are asymmetrical, therefore usually the value of $I(\alpha_T, \beta_T)$ for a specific luminaire and specific range of α_T and β_T can be provided based on measurements campaign to produce what so-called I-table. For

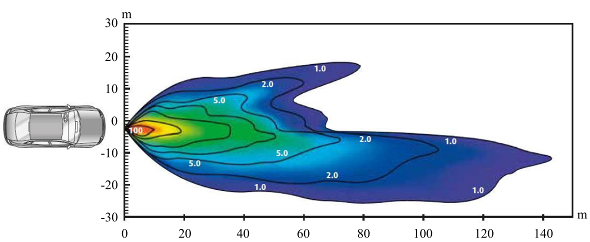

FIGURE 2. An Isolux diagram of a Xenon lamp.

instance, I-table for standard tungsten-halogen headlamp can be found in [13]. Since the commercially available Halogen and Xenon lamps cannot be intensity modulated, whereas no I-table available for advanced LED headlights, we assume that the radiation patterns of both LSH and RSH are following the generalized Lambertian radiation pattern. However, since Lambertian radiation pattern has uniaxial uniformity, this makes it independent of α_T and hence, it can be written as [25]

$$I(\beta_T) = \frac{m+1}{2\pi}\cos^m(\beta_T), \quad \beta_T \in [-\pi/2, \pi/2]. \quad (7)$$

Here, m refers to Lambert's mode number of the optical source, where higher m results in higher light directionality. The irradiance elevation angle is denoted by β_T. As a validation, simulation results in Fig. 3 of a Lambertian pattern showed a good match compared to measurements of a tungsten-halogen low-beam headlamp in [12]. It should be noted that the Tx and Rx have been mounted at a height of 0.6 m.

C. OPTICAL RECEIVER MODEL

The optical receiver can be modeled by its effective area $A_{R_{\text{eff}}}$, which can be expressed as [25]

$$A_{R_{\text{eff}}} = \begin{cases} A_r\cos(\beta_R), & 0 \le \beta_R \le \Psi_{\text{FoV}} \\ 0, & \beta_R > \Psi_{\text{FoV}}. \end{cases} \quad (8)$$

Here, A_r is the area of the PD. The effective area $A_{R_{\text{eff}}}$ guarantees that only the light that received within receiver's field of view (FoV) Ψ_{FoV} will be detected. The effective area can be further extended by attaching a non-imaging

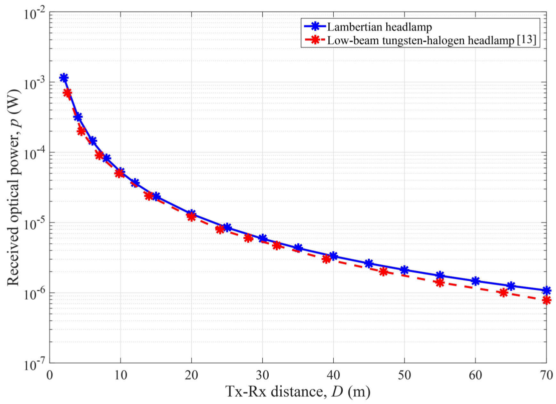

FIGURE 3. Received power when taking into consideration low-beam tungsten-halogen headlamp in [13] and Lambertian headlamp, $h_{\mathrm{Rx}} = 0.6$ m.

concentrator, i.e., a lens to the PD. The optical gain $G(\beta_{\mathrm{R}})$ of the lens is given as [26]

$$G(\beta_{\mathrm{R}}) = \begin{cases} \dfrac{n_{\mathrm{ind}}^2}{\sin^2(\beta_{\mathrm{R}})}, & 0 \leq \beta_{\mathrm{R}} \leq \Psi_{\mathrm{FoV}} \\ 0, & \beta_{\mathrm{R}} > \Psi_{\mathrm{FoV}}. \end{cases} \tag{9}$$

Here, n_{ind} indicates lens refractive index. An optical filter with $T(\beta_{\mathrm{R}})$ transmission coefficient can be also deposited upon the surface of the lens or integrated to be between the lens and the PD. The optical filter is used to block out-of-band natural and artificial light signals. Using a lens alongside with an optical filter will effectively enhance the detectivity of the PD and reduce undesired ambient light, and hence improve SNR significantly.

III. THE 3D RS-GBSM FOR MISO VVLC CHANNELS

In wireless communications, channel modeling plays a key role as accurate characterization of the propagation channel is essential for a robust communication system design and performance evaluation. In conventional RF-based vehicular communications, RS-GBSMs are widely employed to model V2V channels in 2D and 3D [15]–[17], [27]–[29]. Therefore, RS-GBSM is applicable even when a different carrier frequency is used. However, utilizing visible light necessitates careful assumptions to adequately capture VVLC channel characteristics.

Contrast to wireless RF-based channels, wireless optical-based channels offer high robustness against multipath fading [26]. This is due to the spatial diversity that introduced since the typical PD area is in the order of tens of thousands of optical wavelengths and thus no small-scale fading in OWC. Further, employing of IM/DD technique in OWC systems eliminate frequency offset (FO) between the Tx and Rx since no local oscillators involved. Whereas regarding Doppler shift, is has been reported in [30] that the effect of Doppler frequency in OWC systems is negligible. That is due to a slight corresponding wavelength shift which leads to assume that bandwidth spreading and SNR variation due to Doppler are insignificant problems in most IM/DD systems. In spite of the fact that OWC induce a high robustness against multipath fading, optical channels still experience multipath dispersion, which results in intersymbol interference (ISI).

In this study, the wireless optical propagation environment is characterized by a 3D effective scattering with LoS and NLoS components between the Tx and Rx. Fig. 4 and Fig. 5 illustrate the proposed 3D non-stationary RS-GBSM for VVLC MISO channels. This model combines the LoS component, two SB components in two-sphere model, and one SB component in elliptic-cylinder model. For readability purposes, Fig. 4 only shows the geometry of the LoS and SB components in the elliptic-cylinder model. The geometry of the SB components in the two-sphere model is detailed in Fig. 5. In order to describe the proposed model, let us assume that the Txs are surrounded by a sphere of radius R_{T} and there are N_1 effective scatterers are lying on this sphere, where n_1th ($n_1 = 1, \ldots, N_1$) is an effective scatterer denoted by S_{n_1}. Likewise, suppose that the Rx is surrounded by a sphere of radius R_{R} and there are N_2 effective scatterers are lying on this sphere, where n_2th ($n_2 = 1, \ldots, N_2$) is an effective scatterer denoted by S_{n_2}. On the other hand, for the elliptic-cylinder model, we assume that there are N_3 effective scatterers are lying on an elliptic-cylinder. Here, the n_3th ($n_3 = 1, \ldots, N_3$) local scatterer is denoted by S_{n_3}. In the latter model, the mid-distance between the Txs, i.e., OTx and Rx are located at the foci of the elliptic-cylinder. The ellipse parameters a and b (assuming $b < a$) are denoting

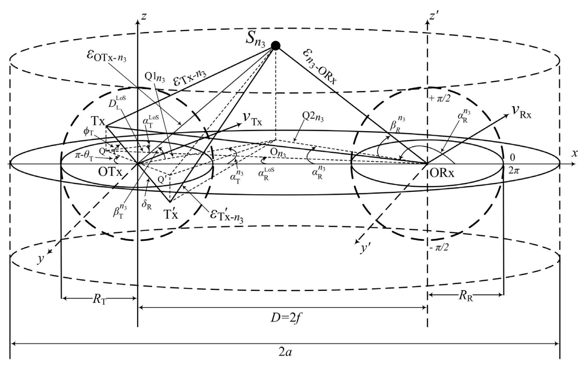

FIGURE 4. The proposed 3D RS-GBSM for VVLC MISO channels (only the LoS and SB components in elliptic-cylinder model).

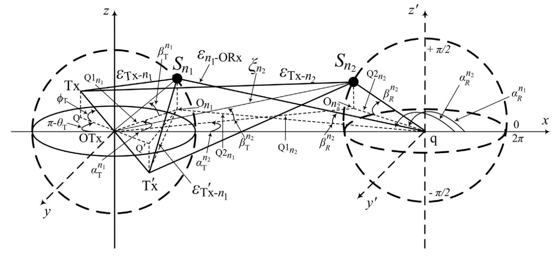

FIGURE 5. The proposed 3D RS-GBSM for VVLC MISO channels (Only the SB rays in the two-sphere model.

TABLE 2. The potential optical ray paths.

Component	Optical Path	Distance
LoS	$\mathrm{Tx}_{\mathrm{L/R}} \to \mathrm{Rx}$	D
1- SB1	$\mathrm{Tx}_{\mathrm{L/R}} \to S_{n_1} \to \mathrm{Rx}$	$\varepsilon_{\mathrm{Tx}-n_1} + \varepsilon_{n_1-\mathrm{ORx}}$, $\varepsilon_{\mathrm{Tx}'-n_1} + \varepsilon_{n_1-\mathrm{ORx}}$
2- SB2	$\mathrm{Tx}_{\mathrm{L/R}} \to S_{n_2} \to \mathrm{Rx}$	$\varepsilon_{\mathrm{Tx}-n_2} + R_{\mathrm{R}}$, $\varepsilon_{\mathrm{Tx}'-n_2} + R_{\mathrm{R}}$
3- SB3	$\mathrm{Tx}_{\mathrm{L/R}} \to S_{n_3} \to \mathrm{Rx}$	$\varepsilon_{\mathrm{Tx}-n_3} + \varepsilon_{n_3-\mathrm{ORx}}$, $\varepsilon_{\mathrm{Tx}'-n_3} + \varepsilon_{n_3-\mathrm{ORx}}$

the semi-major axis and semi-minor axis, respectively. The distance between OTx (mid-distance between Txs) and the Rx is $D = 2f$. Here, f is the half distance between the two focal points of the ellipse and the equality $a^2 = b^2 + f^2$ holds. Here, the focal points (foci) coincide with firstly, the mid-distance between the two headlights at transmission side and secondly, with the position of the Rx at the receiving side. Table 2 presents the potential optical ray paths, while the parameters in Figs. 4 and 5 are defined in Table 3.

To make the proposed 3D RS-GBSM more realistic and practical, two assumptions have been set. Firstly, the bounced rays reflect off the local scatterers from the far to the near relative to the Rx. In other words, the scatterers behind the Tx and prior to the Rx will be neglected. Secondly, ignoring the rays which are out of the PD's FoV Ψ_{FoV}. Consequently, some bounced components will not be necessarily taken into account. Therefore, the total channel gain can be represented as a superposition of the optical waves coming from the direct direction, i.e., LoS and NLoS directions which are determined by the mean direction of the local scatterers, as detailed in next subsections.

A. THE LoS LINK

Since we assume that both LSH and RSH have identical output light patterns, i.e., Lambertian pattern, the detailed derivations for the LoS link contribution will be presented here. For the proposed channel model, the CIR will be deterministic if both the Tx and Rx are static. Accordingly, the received power is proportional to the square of the distance between the Tx and Rx (the inverse square law), PD's area A_{r}, the LoS elevation angle of departure (EAoD) $\beta_{\mathrm{T}}^{\mathrm{LoS}}$, and the LoS elevation angle of arrival (EAoA) $\beta_{\mathrm{R}}^{\mathrm{LoS}}$. Therefore, Eq.(4.6) in [22] can be expressed as

$$h_{\mathrm{L/R}}^{\mathrm{LoS}}(t) = \frac{(m+1)\,G(\beta_{\mathrm{R}})T(\beta_{\mathrm{R}})A_{\mathrm{r}}}{2\pi (D_{\mathrm{L/R}}^{\mathrm{LoS}})^2} \cos^m(\beta_{\mathrm{T,L/R}}^{\mathrm{LoS}}) \times \cos(\beta_{\mathrm{R,L/R}}^{\mathrm{LoS}})\,\delta\Big(t - \frac{D_{\mathrm{L/R}}^{\mathrm{LoS}}}{\mathrm{c}}\Big). \quad (10)$$

Here, $D_{\mathrm{L/R}}^{\mathrm{LoS}} = \sqrt{(\delta_{\mathrm{L/R}})^2 + D^2}$, $\delta(.)$ denotes to the Dirac delta function, $T(\phi_{\mathrm{R}})$ is the transmission coefficient of an optical band-pass filter, $G(\phi_{\mathrm{R}})$ is the gain of the lens, and c is the speed of light. It should be mentioned that we further assumed that both headlights and the PD are equipped at the same height, namely, 0.6 m. Therefore, Eq.(10) was written in terms of the LoS EAoD $\beta_{\mathrm{T}}^{\mathrm{LoS}}$, and EAoA $\beta_{\mathrm{R}}^{\mathrm{LoS}}$. On the other hand, if the Tx and Rx are moving in the same direction, Eq.(10) can be rewritten as

$$h_{\mathrm{L/R}}^{\mathrm{LoS}}(t) = \frac{(m+1)\,G(\beta_{\mathrm{R}})T(\beta_{\mathrm{R}})A_{\mathrm{r}}}{2\pi (D_{\mathrm{TR,L/R}}^{\mathrm{LoS}}(t))^2} \cos^m(\beta_{\mathrm{T,L/R}}^{\mathrm{LoS}}) \times \cos(\beta_{\mathrm{R,L/R}}^{\mathrm{LoS}})\,\delta\Big(t - \frac{D_{\mathrm{TR,L/R}}^{\mathrm{LoS}}(t)}{\mathrm{c}}\Big). \quad (11)$$

Here, $D_{\mathrm{TR,L/R}}^{\mathrm{LoS}}(t)$ indicates the distance between the Txs and Rx as a function of time. Since the LSH and RSH are located at the same distance from the Rx, $D_{\mathrm{TR,L/R}}^{\mathrm{LoS}}(t)$ can be referred as D_{TR} and can be given as

$$D_{\mathrm{TR}}^{\mathrm{LoS}}(t) = \varepsilon_{\mathrm{TR}}(t_0) - [\varepsilon_{\mathrm{Tx}}(t) - \varepsilon_{\mathrm{Rx}}(t)], \quad \upsilon_{\mathrm{Tx}} > \upsilon_{\mathrm{Rx}}. \quad (12)$$

Here, $\varepsilon_{\mathrm{TR}}(t_0)$, $\varepsilon_{\mathrm{Tx}}(t)$, and $\varepsilon_{\mathrm{Rx}}(t)$ indicate initial distance between the Txs and Rx, the distance of the Txs at the given speed after a specific time, and the target Rx distance at the given speed after a specific time, respectively. If we assume that the motion speed of the Tx and Rx vehicles are

TABLE 3. Definition of parameters in Figs. 4 and 5.

D	distance between the center of Tx-sphere and the center of the Rx-sphere
$R_{\mathrm{T}}, R_{\mathrm{R}}$	radius of the Tx and Rx spheres, respectively
2δ	spacing between the LSH and the RSH
a, b	semi-principal axes of the ellipse
$\theta_{\mathrm{T}}, \theta_{\mathrm{R}}$	orientation of the Tx and Rx the x-y plane, respectively
$\phi_{\mathrm{T}}, \phi_{\mathrm{R}}$	elevation of the Tx and Rx relative to the x-y plane, respectively
$\upsilon_{\mathrm{T}}, \upsilon_{\mathrm{R}}$	the speeds of the Tx and Rx, respectively
$\gamma_{\mathrm{T}}, \gamma_{\mathrm{R}}$	moving directions of the Tx and Rx in the x-y plane, respectively
$\alpha_{\mathrm{T}}^{\mathrm{LoS}}, \alpha_{\mathrm{R}}^{\mathrm{LoS}}$	AAoD and AAoA of the LoS paths, respectively
$\alpha_{\mathrm{T}}^{(n_i)} (i = 1, 2)$	azimuth angle of departure (AAoD) from the Tx to the effective scatterers $s^{(n_i)}$
$\alpha_{\mathrm{R}}^{(n_i)} (i = 1, 2)$	azimuth angle of arrival (AAoA) from the effective scatterers $s^{(n_i)}$ to the Rx
$\beta_{\mathrm{T}}^{(n_i)} (i = 1, 2)$	EAoD from the Tx to the effective scatterers $s^{(n_i)}$
$\beta_{\mathrm{R}}^{(n_i)} (i = 1, 2)$	EAoA from the effective scatterers $s^{(n_i)}$ to the Rx
$\varepsilon_{\mathrm{Tx}-n_i}$	distances from the Tx to scatterers $n_i, (i = 1, 2, 3)$
$\xi_{\mathrm{OTx}-n_3}$	distances from the center of Tx-sphere to scatterer n_3
$\xi_{n_i-\mathrm{ORx}}$	distances from scatterer $n_i, (i = 1, 2, 3)$ to the Rx

υ_{Tx} and υ_{Rx}, the motion direction will be determined by the angles of motion γ_{Tx} and γ_{Rx}, respectively, and hence the distances $\varepsilon_{\mathrm{Tx}}(t)$ and $\varepsilon_{\mathrm{Rx}}(t)$, can be written as $\varepsilon_{\mathrm{Tx}}(t) = \upsilon_{\mathrm{Tx}} \times t \times \cos(\gamma_{\mathrm{Tx}})$ and $\varepsilon_{\mathrm{Rx}}(t) = \upsilon_{\mathrm{Rx}} \times t \times \cos(\gamma_{\mathrm{Rx}})$, respectively.

B. THE NLoS LINK

As the number of reflections k_r increases, determining the CIR becomes more complex [31]. However, the contribution of higher k_r to the overall outcome is significantly declining since $\left\| h^{k_r}(t) \right\| \to 0,\ k_r \to \infty$. It has been proven that the primary reflections are dominant over higher order reflections in terms of received power. For instance, indoor measurements have shown that the third bounces carry less than 5% from the total received power in most scenarios. Consequently, only the primary reflections have been considered in this work. Furthermore, unlike indoor VLC, the outdoor environment is a very different and dynamic and hence more affecting the optical wireless channel characteristics. Accordingly, the power of the second reflection will be quite insignificant as has been demonstrated in [14]. Therefore, only the first reflection has been considered in this work. Moreover, to mitigate the complexity of NLoS scenario, the mode number m is assumed to be 1.

1) THE SB TX-SPHERE MODEL

The SB components $h(t)^{(1)}_{\mathrm{L/R}}$ of the CIR within the Tx-sphere model for LSH and RSH can be expressed as

$$\begin{aligned} h^{(1)}_{\mathrm{L/R}}(t) = &\lim_{N_1\to\infty} \sum_{n_1=1}^{N_1} \frac{G(\beta_{\mathrm{R}})T(\beta_{\mathrm{R}})A_{\mathrm{r}}\ \rho_{\mathrm{Vehicles}}}{\pi^2(\varepsilon_{\mathrm{Tx}-n_1})^2\ (\varepsilon_{n_1-\mathrm{ORx}})^2} \\ &\times\cos(\alpha^{(1)}_{\mathrm{T,L/R}})\cos(\beta^{(1)}_{\mathrm{T,L/R}}) \\ &\times\cos(\alpha^{(1)}_{\mathrm{R,L/R}})\cos(\beta^{(1)}_{\mathrm{R,L/R}})\ \delta(t-\frac{\varepsilon^{(1)}_{\mathrm{L/R}}}{\mathrm{c}}). \end{aligned} \tag{13}$$

Referring to Fig. 5, for the LSH, the distance $\varepsilon^{(1)}_{\mathrm{L}}$ in Eq.(13) can be expressed as

$$\varepsilon^{(1)}_{\mathrm{L}} = \varepsilon_{\mathrm{Tx}-n_1} + \varepsilon_{n_1-\mathrm{ORx}}. \tag{14}$$

The distance $\mathrm{OTx} - \mathrm{O_{n_1}}$ $(= Q1_{n_1})$ can be written as $Q1_{n_1} = R_{\mathrm{T}}\ \cos(\beta_{\mathrm{T,L}})$. While the distance $\mathrm{O}_{n_1} - \mathrm{ORx}$ $(= Q2_{n_1})$ is given as

$$Q2_{n_1} = \sqrt{(Q1_{n_1})^2 + 4f^2 - 4f(Q1_{n_1})\cos(\alpha_{\mathrm{T,L}})}. \tag{15}$$

Note that f denotes the distance from the center of the ellipse to each focus. Accordingly, by applying mathematical manipulation, the distance between the LSH and a scatterer, which is lying on the Tx-sphere can be written as

$$\begin{aligned} \varepsilon_{\mathrm{T_x}-n_1} = &(R_{\mathrm{T}}^2 + \delta_L^2 - 2\delta_L R_{\mathrm{T}}\cos(\phi_{\mathrm{T,L}}) \\ &\times\cos(\beta_{\mathrm{T,L}})\cos(\theta_{\mathrm{T,L}} - \alpha_{\mathrm{T,L}}) \\ &- 2\delta_L R_{\mathrm{T}}\sin(\phi_{\mathrm{T,L}})\sin(\beta_{\mathrm{T,L}}))^{0.5}. \end{aligned} \tag{16}$$

While the distance between the above scatterer and the ORx can be given as

$$\varepsilon_{n_1-\mathrm{OR_x}} = Q2_{n_1}/\cos(\beta_{\mathrm{R,L}}). \tag{17}$$

Whilst, with regard to the RSH, the distance between the right headlight and a scatterer, which is lying on the Tx-sphere, can be obtained by applying trigonometry in triangles $\mathrm{OTx}-\mathrm{Q}'-\mathrm{O}_{n_1}$, $\mathrm{Q}'-\mathrm{Tx}'-S_{n_1}$, and $\mathrm{Q}'-\mathrm{Tx}'-\mathrm{O}_{n_1}$ to get

$$\varepsilon_{\mathrm{T_x}'-n_1} = \sqrt{R_{\mathrm{T}}^2 + \delta_R^2 + A1 - B1} \tag{18}$$

where,

$$A1 = 2\ R_{\mathrm{T}}\delta_{\mathrm{T}}\ \sin(\phi_{\mathrm{T,R}})\ \sin(\beta_{\mathrm{T,R}}) \tag{19}$$

and

$$B1 = 2\ R_{\mathrm{T}}\delta_{\mathrm{T}}\ \cos(\phi_{\mathrm{T,R}})\ \cos(\beta_{\mathrm{T,R}})\ \cos(\theta_{\mathrm{T,R}} - \alpha_{\mathrm{T,R}}). \tag{20}$$

It is worth mentioning that the azimuth/elevation angle of departure (AAoD/EAoD), (i.e., $\alpha^{(1)}_{\mathrm{T,L/R}}$, $\beta^{(1)}_{\mathrm{T,L/R}}$) and azimuth/elevation angle of arrival (AAoA/EAoA), (i.e., $\alpha^{(1)}_{\mathrm{R,L/R}}$, $\beta^{(1)}_{\mathrm{R,L/R}}$), are correlated for SB rays. Consequently, a relationship between the AoDs and AoAs can be written as

$$\alpha^{(1)}_{\mathrm{R,L/R}} = \arcsin\left(\frac{R_{\mathrm{T}}\ \cos(\beta_{\mathrm{T,L/R}})\ \sin(\alpha_{\mathrm{T,L/R}})}{\sqrt{(Q1_{n_1})^2+4f^2+4f(Q1_{n_1})\cos(\alpha_{\mathrm{T,L/R}})}}\right) \tag{21}$$

and

$$\beta^{(1)}_{\mathrm{R,L/R}} = \arctan\left(\frac{R_{\mathrm{T}}\ \sin(\beta_{\mathrm{T,L/R}})}{\sqrt{(Q1_{n_1})^2+4f^2+4f(Q1_{n_1})\cos(\alpha_{\mathrm{T,L/R}})}}\right). \tag{22}$$

2) THE SB RX-SPHERE MODEL

The SB components of the CIR $h(t)^{(2)}_{\mathrm{L/R}}$ within the Rx-sphere model for LSH and RSH, can be written as

$$\begin{aligned} h(t)^{(2)}_{\mathrm{L/R}} = &\lim_{N_2\to\infty}\sum_{n_2=1}^{N_2} \frac{G(\beta_{\mathrm{R}})T(\beta_{\mathrm{R}})A_{\mathrm{r}}\ \rho_{\mathrm{Vehicles}}}{\pi(\varepsilon^{(2)}_{\mathrm{L/R}})^2}\cos(\alpha^{n_2}_{\mathrm{T,L/R}}) \\ &\times\cos(\beta^{n_2}_{\mathrm{T,L/R}})\ \cos(\alpha^{n_2}_{\mathrm{R,L/R}})\ \cos(\beta^{n_2}_{\mathrm{R,L/R}}) \\ &\times\delta(t-\frac{\varepsilon^{(2)}_{\mathrm{L/R}}}{\mathrm{c}}). \end{aligned} \tag{23}$$

For the LSH, the distance $\varepsilon^{(2)}_{\mathrm{L}}$ in (23) is given as

$$\varepsilon^{(2)}_{\mathrm{L}} = \varepsilon_{\mathrm{T_x}-n_2} + \mathrm{R_R}. \tag{24}$$

Regarding the optical path lengths within the Rx-sphere model, the distance $\mathrm{OTx} - \mathrm{O}_{n_2}$ $(= Q1_{n_2})$ can be written as

$$Q1_{n_2} = \sqrt{4f^2 + (Q2_{n_2})^2 - 4f(Q2_{n_2})\cos(\alpha_R)}. \tag{25}$$

Here, $Q2_{n_2} = R_{\mathrm{R}}\cos(\beta_{\mathrm{R}})$. Hence,

$$\xi_{n_2} = \sqrt{Q1^2_{n_2} + R^2_{\mathrm{R}}\ \sin^2(\beta_{\mathrm{R}})}. \tag{26}$$

The distance between the LSH and a scatterer, which is lying on the Rx-sphere $\varepsilon_{\mathrm{Tx}-n_2}$, can be obtained by applying

Pythagoras's theorem and the law of sines in the appropriate triangles. Hence, $\varepsilon_{\mathrm{Tx}-n_2}$ can be expressed as

$$\varepsilon_{\mathrm{Tx}-n_2} = \sqrt{A2^2 + B2^2}. \tag{27}$$

Here,

$$A2 = (\delta^2 \cos^2(\phi_{\mathrm{T}}) + (Q1_{n_2})^2 - 2\delta\,(Q1_{n_2})\cos(\phi_{\mathrm{T}})\cos(\theta_{\mathrm{T}} - \alpha_{\mathrm{T}}))^{0.5} \tag{28}$$

and

$$B2 = R_{\mathrm{R}}^2 \sin^2(\beta_{\mathrm{R}}) - 2\delta R_{\mathrm{R}} \sin(\beta_{\mathrm{R}})\sin(\theta_{\mathrm{T}}) + \delta^2 \sin^2(\phi_{\mathrm{T}}). \tag{29}$$

With regard to the RSH, the distance between the RSH and a scatterer that lying on the Rx-sphere $\varepsilon_{\mathrm{T_x}'-n_2}$, can be written as

$$\varepsilon_{\mathrm{T_x}'-n_2} = \sqrt{R_{\mathrm{R}}^2 \sin^2(\beta_{\mathrm{R}}) + \delta^2 \sin^2(\phi_{\mathrm{T}}) + A3 + B3}. \tag{30}$$

Here,

$$A3 = \delta^2 \cos^2(\phi_{\mathrm{T}}) + Q1_{n_2}^2 + 2\delta\, Q1_{n_2} \cos(\phi_{\mathrm{T}})\cos(\theta_{\mathrm{T}} - \alpha_{\mathrm{T}}) \tag{31}$$

and

$$B3 = 2\delta R_{\mathrm{R}} \sin(\phi_{\mathrm{T}})\cos(\beta_{\mathrm{R}}). \tag{32}$$

Since AAoD/EAoD and AAoA/EAoA are correlated for SB rays in Rx-sphere model, the correlation between the AoDs and AoAs is given by

$$\beta_{\mathrm{T,L/R}}^{(2)} = \arcsin\left(\frac{R_{\mathrm{R}} \sin(\beta_{\mathrm{R,L/R}})}{\sqrt{(R_{\mathrm{R}}^2 + 4f^2 + 4fR_{\mathrm{R}}C3}}\right) \tag{33}$$

where,

$$C3 = \cos(\beta_{\mathrm{R,L/R}})\cos(\alpha_{\mathrm{R,L/R}}) \tag{34}$$

and

$$\alpha_{\mathrm{T,L/R}}^{(2)} = \arcsin\left(\frac{R_{\mathrm{R}} \cos(\beta_{\mathrm{R,L/R}})\sin(\alpha_{\mathrm{R,L/R}})}{Q1_{n_2}}\right). \tag{35}$$

3) THE SB ELLIPTIC-CYLINDER MODEL

The SB components $h(t)_{\mathrm{L/R}}^{(3)}$ of the CIR within the elliptic-cylinder model for the LSH and RSH can be expressed as

$$h_{\mathrm{L/R}}^{(3)}(t) = \lim_{N_3\to\infty} \sum_{n_3=1}^{N_3} \frac{G(\beta_{\mathrm{R}})T(\beta_{\mathrm{R}})A_{\mathrm{r}}\, \rho_{\mathrm{Roadside}}}{\pi(\varepsilon_{\mathrm{L/R}}^{(3)})^2} \cos(\alpha_{\mathrm{T,L/R}}^{n_3}) \times\cos(\beta_{\mathrm{T,L/R}}^{n_3})\cos(\alpha_{\mathrm{R,L/R}}^{n_3})\cos(\beta_{\mathrm{R,L/R}}^{n_3}) \times\delta(t - \frac{\varepsilon_{\mathrm{L/R}}^{(3)}}{\mathrm{c}}). \tag{36}$$

For the LSH in Fig. 4, the distance $\varepsilon_{\mathrm{L}}^{(3)}$ in Eq.(36) can be written as

$$\varepsilon_{\mathrm{L}}^{(3)} = \varepsilon_{\mathrm{T_x}-n_3} + \varepsilon_{n_3-\mathrm{OR_x}}. \tag{37}$$

Within the elliptic-cylinder model, the optical path lengths can be determined by using pure elliptic-cylinder properties that mentioned in above. The distance $\mathrm{OTx} - \mathrm{O}_{n_3}$ $(= Q1_{n_3})$ can be expressed as

$$Q1_{n_3} = \sqrt{(Q2_{n_3})^2 + (D)^2 - 2(Q2_{n_3})(D)\cos(\alpha_{\mathrm{R,L}}^{n_3})}. \tag{38}$$

While the distance $\mathrm{O}_{n_3} - \mathrm{ORx}$ $(= Q2_{n_3})$ is given as

$$Q2_{n_3} = \xi_{n_3-\mathrm{ORx}} \cos(\beta_{\mathrm{R,L}}^{n_3}). \tag{39}$$

Based on elliptic-cylinder properties and after some manipulation we can get

$$\varepsilon_{n_3-\mathrm{ORx}} = \frac{2a - Q_{n_3}}{\cos(\beta_{\mathrm{R,L}}^{n_3})} \tag{40}$$

and

$$\varepsilon_{\mathrm{OTx}-n_3} = \sqrt{Q_{n_3}^2 + (\xi_{n_3-\mathrm{ROx}})^2 \sin^2(\beta_{\mathrm{R,L}}^{n_3})} \tag{41}$$

where

$$Q_{n_3} = \frac{a^2 + f^2 + 2af\,\cos(\alpha_{\mathrm{R,L}}^{n_3})}{a + f\,\cos(\alpha_{\mathrm{R,L}}^{n_3})}. \tag{42}$$

The distance between the LSH and a scatterer that lying on the elliptic-cylinder model $\varepsilon_{\mathrm{T_x}-n_3}$, can be written as

$$\varepsilon_{\mathrm{Tx}-n_3} = \sqrt{A4^2 + B4^2}. \tag{43}$$

Here,

$$A4 = \delta^2 + Q1_{n_3}^2 - 2\delta\, Q1_{n_3} \cos(\phi_{\mathrm{T}})\cos(\theta_{\mathrm{T}} - \alpha_{\mathrm{T}}) \tag{44}$$

and

$$B4 = \delta^2 + \varepsilon_{n_3-\mathrm{ORx}}^2 \sin^2(\beta_{\mathrm{R}}) - 2\delta\, \varepsilon_{n_3-\mathrm{ORx}} \times\sin(\beta_{\mathrm{R}})\sin(\phi_{\mathrm{T}}). \tag{45}$$

For the RSH, the distance between the RSH and a scatterer that lying on the elliptic-cylinder model $\varepsilon_{\mathrm{T_x}'-n_3}$, can be written as

$$\varepsilon_{\mathrm{T_x}'-n_3} = \sqrt{\delta^2 \sin^2(\phi_{\mathrm{T}}) + A5 - B5}. \tag{46}$$

Here,

$$A5 = D^2 + \varepsilon_{n_3-\mathrm{ORx}}^2 - 2D\,\varepsilon_{n_3-\mathrm{ORx}} \cos(\beta_{\mathrm{R}})\cos(\alpha_{\mathrm{R}}) \tag{47}$$

and

$$B5 = 2D\delta\varepsilon_{n_3-\mathrm{ORx}} \sin(\phi_{\mathrm{T}})\cos(\alpha_{\mathrm{R}}). \tag{48}$$

Since the correlation between AAoD/EAoD and AAoA/EAoA is still valid in elliptic-cylinder model, the relationship between the AAoAs and AAoDs can be expressed as

$$\beta_{\mathrm{T,L/R}}^{(3)} = \arcsin\left(\frac{\varepsilon_{n_3-\mathrm{ORx}} \sin(\beta_{\mathrm{R,L/R}})}{\varepsilon_{\mathrm{OTx}-n_3}}\right). \tag{49}$$

While the relationship between the EAoAs and EAoDs can be written as

$$\alpha_{\mathrm{T,L/R}}^{(3)} = \arcsin\left(\frac{\varepsilon_{n_3-\mathrm{ORx}} \cos(\beta_{\mathrm{R,L/R}})\sin(\alpha_{\mathrm{R,L/R}})}{Q1_{n_3}}\right). \tag{50}$$

IV. VVLC CHANNEL CHARACTERISTICS

A. VON MISES FISHER DISTRIBUTION (VMF)

Theoretical RS-GBSMs assume infinite number of effective scatterers and hence infinite complexity. However, in this study, only the discrete AAoD $\alpha_{\mathrm{T}}^{(n_i)}$, EAoD $\beta_{\mathrm{T}}^{(n_i)}$, AAoA $\alpha_{\mathrm{R}}^{(n_i)}$, and EAoA $\beta_{\mathrm{R}}^{(n_i)}$ will be considered. The methodology of obtaining the set of $\left\{\alpha^{(n_i)}, \beta^{(n_i)}\right\}$ will be given in the next section. In order to consider the joint impact of the azimuth and elevation angles on channel properties, VMF probability density functions (PDF) is used in this paper to represent the concentration of the effective scatterers. VMF distribution is commonly used to describe directional data and parameterized by a mean direction and a concentration factor k. VMF PDF is defined as [32]

$$f(\alpha,\beta)=\frac{k\cos\beta}{4\pi\sinh k}e^{k[\cos\beta_0\cos\beta\cos(\alpha-\alpha_0)+\sin\beta_0\sin\beta]}. \quad (51)$$

Here, $\alpha\in(-\pi,\pi)$ and $\beta\in(-\pi/2,\pi/2)$, while $\alpha_0\in(-\pi,\pi)$ and $\beta_0\in(-\pi/2,\pi/2)$ refer to the mean values of the azimuth angle α and elevation angle β, respectively. The k ($k\geqslant 0$) parameter is a real-valued parameter which characterizes the concentration of the local scatterers relative to the mean direction, i.e., α_0 and β_0. In order to demonstrate the VMF on the unit sphere in 3D space, we set $\alpha_0=10°$, $\beta_0=2°$, and $k=30$ as an example and plot the scatterers (10000 points) that embedded in a 3D Euclidean space to obtain the distribution that shown in Fig. 6(a). While Fig. 6(b) illustrates the corresponding VMF PDF. According to VMF distribution, higher values of k imply higher concentration around the direction of the mean angles [33]. In consequence, $k\to 0$ produces an isotropic distribution, while for $k\to\infty$ the distribution will be extremely non-isotropic.

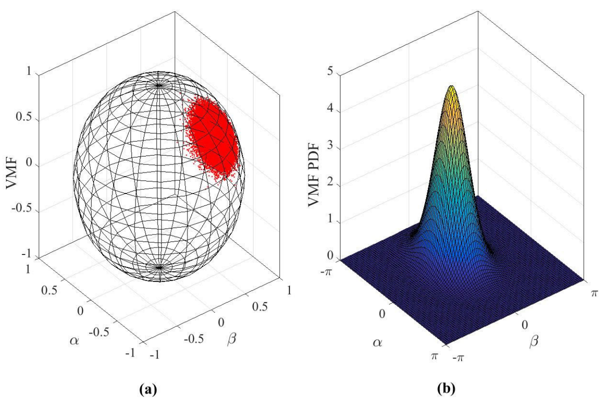

FIGURE 6. (a) The VMF distribution on the unit sphere in 3D and (b) VMF PDF ($\alpha_0=10°$, $\beta_0=2°$, $k=30$).

B. CHANNEL DC GAIN

Let us consider LSH and RSH with Lambertian sources, a receiver with an optical band-pass filter of transmission $T(\phi_{\mathrm{R}})$ and a lens of gain $G(\phi_{\mathrm{R}})$, the channel DC gain for the LoS links can be expressed as

$$H(0)_{\mathrm{L/R}}^{\mathrm{LoS}}=\begin{cases}\dfrac{G(\beta_{\mathrm{R}})T(\beta_{\mathrm{R}})A_{\mathrm{r}}}{\pi(D_{\mathrm{TR,L/R}}^{\mathrm{LoS}})^2}\\ \times\cos(\beta_{\mathrm{T,L/R}}^{\mathrm{LoS}})\cos(\beta_{\mathrm{R,L/R}}^{\mathrm{LoS}}) & 0<\beta_{\mathrm{R,L/R}}\leqslant\Psi_{\mathrm{FoV}}\\ 0 & \beta_{\mathrm{R,L/R}}>\Psi_{\mathrm{FoV}}.\end{cases} \quad (52)$$

On the other hand, in order to consider the joint effect of azimuth and elevation angles on the optical wireless channel for the NLoS scenario, we need to consider the gain of all reflected paths by performing the double integral of the 3D VMF PDF, i.e., the volume of Fig. 6(b). Therefore, channel DC gain of LSH and RSH for the NLoS scenario can be written as

$$H(0)_{\mathrm{L/R}}^{\mathrm{SB}}=\begin{cases}\displaystyle\int_{-\pi/2}^{\pi/2}\int_{-\pi/2}^{\pi/2}I_{L,R}(\alpha,\beta)\\ \times h_{L,R}(t)\\ \times f_{L,R}(\alpha,\beta)\,d\alpha\,d\beta & 0<\beta_{\mathrm{R,L/R}}\leqslant\Psi_{\mathrm{FoV}}\\ 0 & \beta_{\mathrm{R,L/R}}>\Psi_{\mathrm{FoV}}.\end{cases} \quad (53)$$

Here, $f_{L,R}(\alpha,\beta)$ denotes VMF PDF. It is worth noting that here we apply the second criteria in Section III to exclude the rays which are out of the PD's FoV.

C. NOISE MODELING

For outdoor VLC applications, the optical noise can be produced by background light from solar light during the daytime and other artificial lights such as streetlights, vehicles lights, and advertising screens at nighttime [12]. Optical noise is a decisive factor in determining link performance. The total noise at the Rx side is comprised of firstly, the noise that induced by the photocurrent which is known as shot noise σ_{sh}^2. Secondly, the noise that resulting from the ambient light sources, i.e., background noise σ_{b}^2. The third type of noise is dark current noise σ_{d}^2, which is the reverse leakage current induced by a random generation of electrons and holes through the PD in the absence of light. Forthly, the thermal noise σ_{th}^2, which is induced by the receiver's electronics such as the resistive elements [34]. Consequently, the total noise variance is defined as [26]

$$\sigma_{\mathrm{total}}^2=\sigma_{\mathrm{sh}}^2+\sigma_{\mathrm{b}}^2+\sigma_{\mathrm{d}}^2+\sigma_{\mathrm{th}}^2. \quad (54)$$

The shot noise and thermal noise variances are expressed as [26]

$$\sigma_{\mathrm{sh}}^2=2qR_\lambda P_{\mathrm{Rx}}B+2qI_BI_2B \quad (55)$$

and

$$\sigma_{\mathrm{th}}^2=\frac{8\pi k_{\mathrm{B}}T_{\mathrm{k}}}{G_{\mathrm{ol}}}C_{\mathrm{PD}}A_{\mathrm{r}}I_2B^2+\frac{16\pi^2k_{\mathrm{B}}T_{\mathrm{k}}\Gamma}{g_{\mathrm{m}}}C_{\mathrm{PD}}A_{\mathrm{r}}^2I_3B^3, \quad (56)$$

respectively. The other noise contributions in Eq.(54) can be obtained according to [26] (Eq.(4.7)). In this paper, we have adopted IM/DD that employing on-off keying (OOK) scheme. Therefore, the SNR at the receiver side is given as [26]

$$\mathrm{SNR} = \frac{(R_\lambda\, P_{\mathrm{Rx}})^2}{\sigma^2_{\mathrm{total}}}. \tag{57}$$

V. SIMULATION RESULTS AND ANALYSIS

In performing simulations, the key parameters for the proposed system model are summarized in Table 4. The most cars have bodies made from either steel or aluminum. For painted steel bodies, the average reflectance ρ_{Vehicles} will be taken into account. On the other hand, for the roadside environment, average concrete reflectance ρ_{Roadside} has been selected. The most important VVLC channel characteristics have been studied in below subsections.

TABLE 4. Values of model key parameters used in the simulations.

Model Key Parameters	
Initial Tx-Rx distance	70 m
Semi-major a & semi-minor b axes	40 m, 19 m
Tx speed υ_{Tx}	21.6 km/h
Rx speed υ_{Rx}	14.4 km/h
Sphere Radius $(R_{\mathrm{T}}, R_{\mathrm{R}})$	4 m
Lane width	3.5 m [35]
Roadside width	2.2 m [36]
Stopping distance (SD)	6 m [37]
Vehicles Reflectivity (ρ_{Vehicles})	0.8 [38]
Roadside Reflectivity (ρ_{Roadside})	0.4 [39]
PD Area	1 cm^2
Refractive index (n_{ind})	1.5
Optical filter gain ($T(\beta_{\mathrm{R}})$)	1
Luminous intensity (I)	8830 cd [13]
PD Field of view (FoV)	80°
Number of Scatterers	100
Capacitance of PD per unit area (C_{PD})	112 pF/cm^2 [40]
Noise bandwidth factors I_2 and I_3	0.562 and 0.0868 [12]
FET channel noise factor (Γ)	1.5 [26]
Boltzmann's constant (k_{B})	1.38×10^{-23} J/K
Absolute temperature (T_{k})	298 K
Electric charge (q)	1.6×10^{-19} C
Open-loop voltage gain (G_{ol})	10 [12]
FET transconductance (g_{m})	30 mS [41]
VLC system bandwidth (B)	20 MHz
Background noise current (I_{B})	5100 μA [40]

A. RECEIVED OPTICAL POWER

In this section, the received wireless optical power is analyzed based on the proposed VVLC MISO channel model parameters.

1) LoS COMPONENTS

In this model we consider that the Tx and Rx are moving in the same direction. Since the drivers try to keep the car centered in the current lane, we assume that the reference projection of the Tx vehicle is the lane's center as shown in Fig. 1. The target vehicle Rx can be located either in the same lane or in an adjacent lane. The received power will be determined mainly by the Tx-Rx distance. For simulation purposes, we have set the following values for the main model parameters. The initial distance (at $t = 0$) between the Tx vehicle and Rx vehicle is 70 m and they are moving with speed of 6 m/s (21.6 km/h) and 4 m/s (14.4 km/h), respectively, in the same direction, i.e., $\gamma_{\mathrm{Tx}} = \gamma_{\mathrm{Rx}} = 0$. Here, the headlight separation 2δ is 1.20 m [12]. As the Tx vehicle is moving at higher speed than the Rx vehicle, we assumed that the stopping distance (SD) is 6 m [37]. By considering above parameters and applying Eq.(11) and Eq.(12), the simulation results are shown in Fig. 7. This figure illustrates the contribution of each headlight in addition to the total received power, which is the sum of the LSH and RSH powers. It can be seen that the received power depends on the Tx-Rx distance and this behavior becomes more pronounced when the Tx and Rx get closer to each other.

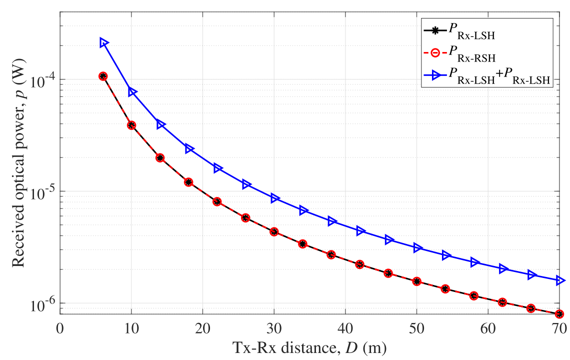

FIGURE 7. Received power of LoS components vs. Tx-Rx distance ($\upsilon_{\mathrm{Tx}} = 21.6$ km/h, $\upsilon_{\mathrm{Rx}} = 14.4$ km/h, $\gamma_{\mathrm{T}} = \gamma_{\mathrm{R}} = 0°$, $2\delta = 1.2$ m, $\phi_{\mathrm{T}} = 0°$, SD = 6 m, $m = 1$).

On the other hand, we considered the generalized Lambertian radiation pattern because there is no available measured beam pattern for a standard LED headlamp. Therefore, we examine the effect of mode number m of Lambertian radiation pattern on the received optical power. By taking into account the total received power from both LSH and RSH, it has been demonstrated that the received power increases as the mode number increases as illustrated in Fig. 8. This is due to the fact that higher mode number provides higher directionality of the optical source and hence more power will be delivered.

2) THE SB COMPONENTS

In this work, the VMF distribution have been adopted to take into account the joint impact of both azimuth and elevation angles on the channel characteristics. Since no measurements available, the main parameters including the mean values of the azimuth angles $\alpha_0^{(i)}$ and elevation angles $\beta_0^{(i)}$ $(i = 1, 2, 3)$, as well as the concentration factor k will be assumed for simulation purposes. Accordingly, the related propagation

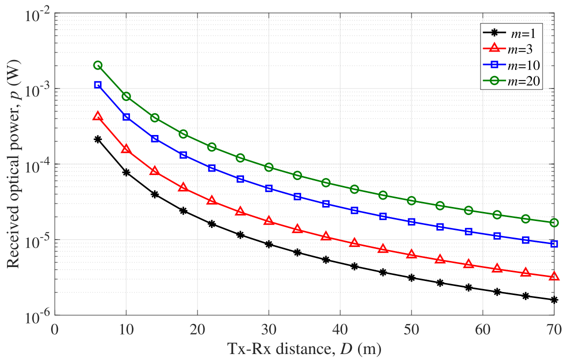

FIGURE 8. Received power of LoS components vs. Tx-Rx distance ($v_{\mathrm{Tx}} = 21.6$ km/h, $v_{\mathrm{Rx}} = 14.4$ km/h, $\gamma_{\mathrm{T}} = \gamma_{\mathrm{R}} = 0°$, $2\delta = 1.2$ m, $\phi_{\mathrm{T}} = 0°$, SD = 6 m, $m = 1, 3, 10, 20$).

distances can be determined by using the derived equations that are presented in Sections III and IV. Here, we tried to make the assumptions as much as close to the reality. Since the effective scatterers are distributed according to the VMF distribution, we will investigate and analyze the effect of VMF parameters on the received power, namely, $N^{(i)}$, $k^{(i)}$, $\alpha^{(n_i)}$, and $\beta^{(n_i)}$. For simulation purposes, appropriate values for the numbers of discrete scatterers $N^{(i)}$ must be chosen carefully [42]. Based on our own simulation experiences, the value for $N^{(i)}$ is set to be 100. Furthermore, in order to obtain the set of $\left\{\alpha^{(n_i)}, \beta^{(n_i)}\right\}_{n_i=1}^{N_i}$ we use the method of equal volume (MEV), which is proposed in [17] to generate discrete values for the azimuth and elevation angles around the mean direction. In the following subsections, the effect of each parameter on the received power is studied separately for each model.

a: RECEIVED OPTICAL POWER FROM TX-SPHERE AND RX-SPHERE MODELS

The received power is related to the concentration factor k, which is managing the distribution of the scatterers according to VMF distribution. In this paper, we examine the impact of k and the mean direction of the scatterers on the power amount that can be received from LSH and RSH. Here, the mean direction of the scatterers indicates the position of a car in the adjacent lane. In reality, vehicles are not aligned precisely with other surrounding vehicles that located in the adjacent lanes. Hence, cars which are on the right side make different angles compared with the cars on the left side. In order to consider the cars on the left side and right sides, two sets of mean angles have been defined, $\left\{\alpha_0^{(n_i,\mathrm{L})}, \beta_0^{(n_i,\mathrm{L})}\right\}$ and $\left\{\alpha_0^{(n_i,\mathrm{R})}, \beta_0^{(n_i,\mathrm{R})}\right\}$, respectively. As VVLC technology is still growing and at an early stage of research, there are currently no available measurements data. Therefore, we tried to take into account the most reliable parameters which are as close to reality as possible and hence we set the value of the elevation angle to 2°. This is due to the fact that in urban environments, the majority of cars will be sedan cars and hence the reflection from the surrounding cars will be at almost the same plane. On the other hand, the azimuth angles have been set to values as $\alpha_0^{(n_i,\mathrm{L})} = \alpha_0^{(n_i,\mathrm{R})} = 10°, 30°, 45°$. The azimuth angles were chosen to ensure that the most probable positions for the adjacent cars have been taken into account. Furthermore, regarding $k_{\mathrm{c}}^{(i)}$, we followed the procedure that used in conventional RF V2V scenarios in [17]. However, for VVLC, the value of $k_{\mathrm{c}}^{(i)}$ has been set to 3, 14, and 30. The other parameters which are related to the proposed model are listed in Table 4. Since the LSH and RSH present the same behavior, here only the powers which are generated at LSH and reflected off the surrounding vehicles on the left side will be analyzed. Fig. 9 and Fig. 10 illustrate the received power from LSH within Tx-Sphere model and Rx-Sphere model, respectively. It can be realized that higher optical power will be received as k goes higher. This is due that the higher k means the local scatterers are being highly aligned around the mean angles. On the other hand, when the mean angles increase, the received power decrease. For instance, in Fig. 9, for $k = 30$ the received power from the LSH that reflected off an obstacle located at the left side at a distance of 10 m is 3.37×10^{-8} W when the mean angle $\alpha_0^{(1)} = 10°$. While the received power is 1.45×10^{-8} W when $\alpha_0^{(1)} = 45°$, for the same k value. This is due to Lambert's cosine law as the light intensity is correlated to the angle with surface normal of the

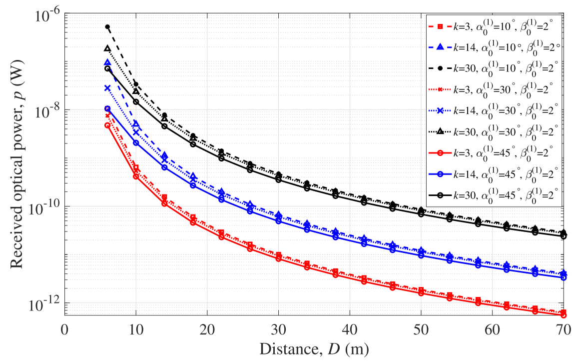

FIGURE 9. Received power from LSH within Tx-Sphere model ($\gamma_T = \gamma_R = 0°$, $\delta = 0.6$ m, $\phi_{\mathrm{T}} = 0$, $\alpha_0^{(1)} = 10°, 30°, 45°$, $\beta_0^{(1)} = 2°$, $k = 3, 10, 30$).

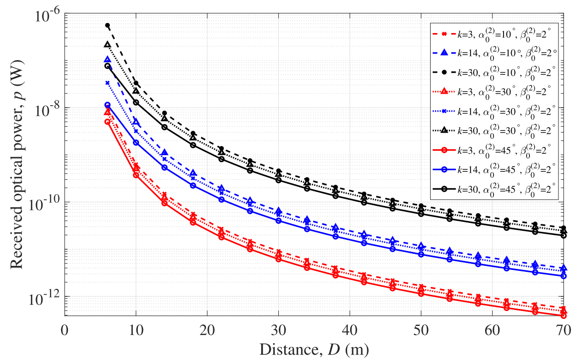

FIGURE 10. Received power from LSH within Rx-Sphere model ($\gamma_T = \gamma_R = 0°$, $\delta = 0.6$ m, $\phi_{\mathrm{T}} = 0$, $\alpha_0^{(2)} = 10°, 30°, 45°$, $\beta_0^{(2)} = 2°$, $k = 3, 10, 30$).

LED headlight and PD. Furthermore, as much as k decreases, there will be no dominant mean direction and hence more deviation about the surface normal.

It is worth mentioning that in terms of Rx-sphere model, the FoV constraint of the PD is considered. Consequently, the assumed mean angles, i.e., $\alpha_0^{(2)}$, and $\beta_0^{(2)}$ must be within PD's FoV Ψ_{FoV}.

b: RECEIVED OPTICAL POWER FROM ELLIPTIC-CYLINDER MODEL

In terms of the elliptic-cylinder model, it is intuitive that less power will be received compared with the two-sphere model. This is due to two main reasons, firstly, the lower reflectivity of the roadside environments ρ_{Roadside}. Secondly, the longer optical path lengths within the elliptic-cylinder model. In this case, the same behavior which is noticed in the Tx- and Rx-sphere appears here so that higher k produces much power at the PD. Fig. 11 illustrates the received optical power, which is transmitted from LSH then reflected off the roadside environments to be detected by the PD. For SB components, it can be noted from the above figures that at distances shorter than 10 m, the model cannot simulate satisfactorily the behavior of the wireless optical channel since some results are overlapped. This is due the radius of the Tx and Rx spheres, since no applicable reflection can be occurred at the range of 8 m.

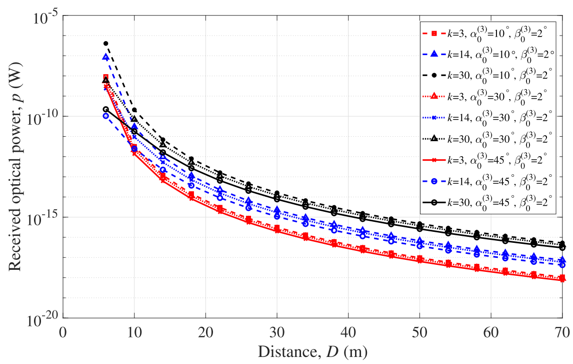

FIGURE 11. Received power from LSH within elliptic-cylinder model ($\gamma_T = \gamma_R = 0°$, $\delta = 0.6$ m, $\phi_T = 0$, $\alpha_0^{(3)} = 10°, 30°, 45°$, $\beta_0^{(3)} = 2°$, $k = 3, 10, 30$).

On the other hand, in order to show the amount of power added by the SB components, Fig. 12 illustrates the LoS power in addition to SB power of the LSH. It can be seen that the LoS component plays a decisive role in the received optical power and the SB components add insignificant amounts of added powers, especially at longer Tx-Rx distances. In addition, the power difference between the LoS component and SB component increases as the Tx-Rx distance increases.

B. SNR

Based on the noise analysis in Section IV–C, the performance of each component can be analyzed through the relationship between the SNR and Tx-Rx distance as illustrated in Fig. 13. Here, only the assumption of $\alpha_0^{(i)} = 10°$, $\beta_0^{(i)} = 2°$, and $k = 30$ has been considered for all components. This is due to the fact that these components carry higher power compared with the others. It can be noticed from Fig. 13, that SNR values decrease as the Tx-Rx distances increase and the difference in received power according to each component is maintained.

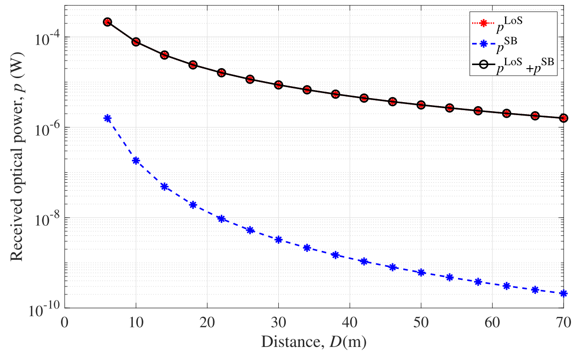

FIGURE 12. The received power of LoS and SB components of LSH ($k = 30, \alpha_0^{(i)} = 30°,\ \beta_0^{(i)}, = 2°, i = 1, 2, 3$).

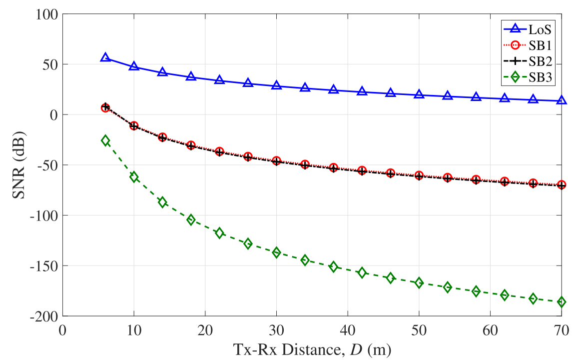

FIGURE 13. SNR vs. Tx-Rx distance ($k = 30, \alpha_0^{(i)} = 10°, \beta_0^{(i)}, = 2°$, $i = 1, 2, 3$).

C. COMPARISON BETWEEN 3D VVLC RS-GBSM AND 2D VVLC RS-GBSM

Regarding the proposed 3D RS-GBSM, it is worth to emphasize that when $\beta^{(n_i)} = 0$, $(i = 1, 2, 3)$, the proposed 3D model will be reduced to a 2D RS-GBSM (two-ring and elliptic model) in [14]. In order to evaluate the impact of elevation angle on the received power, Fig. 14 and Fig.15 illustrate comparisons between the 3D and 2D models in terms of the received power from LSH for the LoS and SB components, respectively. Note that we considered the same number of effective scatterers, i.e., $N = 100$. From Fig.14 and Fig.15, it is clear that compared with the 3D model, the 2D model overestimates the received optical power. The reason is that the 2D model assumes that $\beta^{(n_i)}$ has no contribution. Moreover, compared to the 2D model in [14], 3D model introduces an extra optical path length caused by considering the headlight separation 2δ.

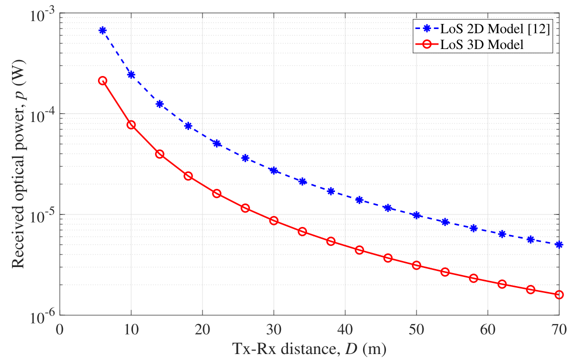

FIGURE 14. **LoS received power comparison between the 3D and 2D models ($\upsilon_{Tx} = 21.6$ km/h, $\upsilon_{Rx} = 14.4$ km/h, $\gamma_T = \gamma_R = 0°$, $2\delta = 1.2$ m, $\phi_T = 0°$, $m = 1$).**

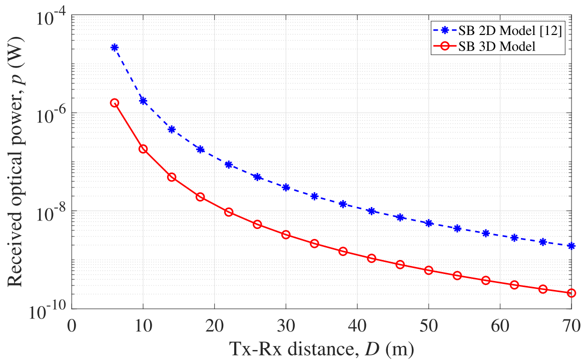

FIGURE 15. **SB received power comparison between the 3D and 2D models ($\upsilon_{Tx} = 21.6$ km/h, $\upsilon_{Rx} = 14.4$ km/h, $\gamma_T = \gamma_R = 0°$, $2\delta = 1.2$ m, $\phi_T = 0°$, $m = 1$).**

VI. CONCLUSION

In this paper, a new 3D non-stationary RS-GBSM for VVLC MISO channels has been proposed. The proposed model jointly considers the azimuth and elevation angles by using the VMF distribution. VVLC channel characteristics have been examined through a large set of channel impulse responses generated by the proposed 3D RS-GBSM. The received optical powers for the LoS and SB components have been computed along different distance ranges between 0 and 70 m. Simulation results have shown that for the proposed model, the azimuth angle has a significant impact on the received power. This is due to the fact that light intensity is correlated with the cosine of the observation angle with respect to the surface normal of the LED headlight and PD. Moreover, the background noise sources have been modeled and the VVLC system's SNR has been evaluated accordingly. Finally, it has been demonstrated that compared with the 3D model, the 2D model overestimates the received optical power.

REFERENCES

[1] *World Health Organization*. Accessed: Mar. 30, 2020. [Online]. Available: http://www.who.int/mediacentre/factsheets/fs358/en/

[2] S. Zeadally, R. Hunt, Y.-S. Chen, A. Irwin, and A. Hassan, "Vehicular ad hoc networks (VANETS): Status, results, and challenges," *Telecommun. Syst.*, vol. 50, no. 4, pp. 217–241, Aug. 2012.

[3] C.-X. Wang, F. Haider, X. Gao, X.-H. You, Y. Yang, D. Yuan, H. Aggoune, H. Haas, S. Fletcher, and E. Hepsaydir, "Cellular architecture and key technologies for 5G wireless communication networks," *IEEE Commun. Mag.*, vol. 52, no. 2, pp. 122–130, Feb. 2014.

[4] A. Al-Kinani, "Channel modelling for visible light communication systems," Ph.D. dissertation, School Eng. Phys. Sci., Heriot-Watt University, Edinburgh, U.K., 2018. [Online]. Available: https://www.ros.hw.ac.uk/handle/10399/3486

[5] A. Al-Kinani, C.-X. Wang, H. Haas, and Y. Yang, "A geometry-based multiple bounce model for visible light communication channels," in *Proc. IEEE IWCMC*, Paphos, Cyprus, Sep. 2016, pp. 31–37.

[6] M. Wada, T. Yendo, T. Fujii, and M. Tanimoto, "Road-to-vehicle communication using LED traffic light," in *IEEE Intell. Veh. Symp.*, Las Vegas, NV, USA, Jun. 2005, pp. 601–606.

[7] G. Pang, T. Kwan, H. Liu, and C.-H. Chan, "LED wireless," *IEEE Ind. Appl. Mag.*, vol. 8, no. 1, pp. 21–28, Jan. 2002.

[8] S. Iwasaki, C. Premachandra, T. Endo, T. Fujii, M. Tanimoto, and Y. Kimura, "Visible light road-to-vehicle communication using high-speed camera," in *Proc. IEEE Intell. Veh. Symp.*, Eindhoven, The Netherlands, Jun. 2008, pp. 13–18.

[9] S. J. Lee, J. K. Kwon, S. Y. Jung, and Y. H. Kwon, "Simulation modelling of visible light communication channel for automotive applications," in *Proc. IEEE ITSC*, Anchorage, AK, USA, Sep. 2012, pp. 463–468.

[10] S. Lee, J. K. Kwon, S.-Y. Jung, and Y.-H. Kwon, "Evaluation of visible light communication channel delay profiles for automotive applications," *EURASIP J. Wireless Commun. Netw.*, vol. 2012, no. 1, pp. 1–8, Dec. 2012.

[11] A. Al-Kinani, C.-X. Wang, L. Zhou, and W. Zhang, "Optical wireless communication channel measurements and models," *IEEE Commun. Surveys Tuts.*, vol. 20, no. 3, pp. 1939–1962, 3rd Quart., 2018.

[12] P. Luo, Z. Ghassemlooy, H. L. Minh, E. Bentley, A. Burton, and X. Tang, "Performance analysis of a car-to-car visible light communication system," *Appl. Opt.*, vol. 54, no. 7, pp. 1696–1706, Mar. 2015.

[13] B. Schoettle and M. J. Flannagan, "A market-weighted description of low-beam and high-beam headlighting patterns in the U.S.," Univ. Michigan, Ann Arbor, MI, USA, Tech. Rep. UMTRI-2004-23, 2004.

[14] A. Al-Kinani, J. Sun, C.-X. Wang, W. Zhang, X. Ge, and H. Haas, "A 2-D non-stationary GBSM for vehicular visible light communication channels," *IEEE Trans. Wireless Commun.*, vol. 17, no. 12, pp. 7981–7992, Dec. 2018.

[15] Y. Yuan, C.-X. Wang, Y. He, M. M. Alwakeel, and E.-H.-M. Aggoune, "3D wideband non-stationary geometry-based stochastic models for non-isotropic MIMO vehicle-to-vehicle channels," *IEEE Trans. Wireless Commun.*, vol. 14, no. 12, pp. 6883–6895, Dec. 2015.

[16] S. Wu, C.-X. Wang, E.-H.-M. Aggoune, M. M. Alwakeel, and X. You, "A general 3-D non-stationary 5G wireless channel model," *IEEE Trans. Commun.*, vol. 66, no. 7, pp. 3065–3078, Jul. 2018.

[17] Y. Yuan, C.-X. Wang, X. Cheng, B. Ai, and D. I. Laurenson, "Novel 3D geometry-based stochastic models for non-isotropic MIMO vehicle-to-vehicle channels," *IEEE Trans. Wireless Commun.*, vol. 13, no. 1, pp. 298–309, Jan. 2014.

[18] C.-X. Wang, X. Cheng, and D. Laurenson, "Vehicle-to-vehicle channel modeling and measurements: Recent advances and future challenges," *IEEE Commun. Mag.*, vol. 47, no. 11, pp. 96–103, Nov. 2009.

[19] V. Dixit, S. Shukla, and M. Shukla, "Performance analysis of optical IDMA system for indoor wireless channel model," in *Proc. IEEE CICN*, Mathura, India, Nov. 2012, pp. 382–386.

[20] J. Maurer, T. Fuegen, and W. Wiesbeck, "A ray-optical channel model for vehicular ad-hoc networks," in *Proc. IEEE EW*, Nicosia, Cyprus, Apr. 2005, pp. 1–7.

[21] J. R. Barry, J. M. Kahn, W. J. Krause, E. A. Lee, and D. G. Messerschmitt, "Simulation of multipath impulse response for indoor wireless optical channels," *IEEE J. Sel. Areas Commun.*, vol. 11, no. 3, pp. 367–379, Apr. 1993.

[22] J. R. Barry, *Wireless Infrared Communications*. New York, NY, USA: Springer, 1994.

[23] D. Hynd, M. McCarthy, J. Carroll, M. Seidl, M. Edwards, C. Visvikis, M. Tress, N. Reed, and A. Stevens, "Benefit and feasibility of a range of new technologies and unregulated measures in the fields of vehicle occupant safety and protection of vulnerable road users," Eur. Commission, Brussels, Belgium, Tech. Rep., 2015. Accessed: Mar. 31, 2020. [Online]. Available: https://op.europa.eu/en/publication-detail/-/publication/47beb77e-b33e-44c8-b5ed-505acd6e76c0

[24] J. L. Lindsey, *Applied Illumination Engineering*, 2nd ed. Lilburn GA, USA: Fairmont Press, 1997.

[25] F. R. Gfeller and U. Bapst, "Wireless in-house data communication via diffuse infrared radiation," *Proc. IEEE*, vol. 67, no. 11, pp. 1474–1486, Nov. 1979.
[26] Z. Ghassemlooy, W. Popoola, S. Rajbhandari, *Optical Wireless Communications: System and Channel Modelling With MATLAB*. New York, NY, USA: CRC Press, 2013.
[27] X. Cheng, C.-X. Wang, D. Laurenson, S. Salous, and A. Vasilakos, "An adaptive geometry-based stochastic model for non-isotropic MIMO mobile-to-mobile channels," *IEEE Trans. Wireless Commun.*, vol. 8, no. 9, pp. 4824–4835, Sep. 2009.
[28] Q. Zhu, W. Li, C.-X. Wang, D. Xu, J. Bian, X. Chen, and W. Zhong, "Temporal correlations for a non-stationary Vehicle-to-Vehicle channel model allowing velocity variations," *IEEE Commun. Lett.*, vol. 23, no. 7, pp. 1280–1284, Jul. 2019.
[29] C.-X. Wang, J. Bian, J. Sun, W. Zhang, and M. Zhang, "A survey of 5G channel measurements and models," *IEEE Commun. Surveys Tuts.*, vol. 20, no. 4, pp. 3142–3168, 4th Quart., 2018.
[30] H. Elgala, R. Mesleh, and H. Haas, "Practical considerations for indoor wireless optical system implementation using OFDM," in *Proc. ConTEL*, Zagreb, Croatia, Jun. 2009, pp. 25–29.
[31] V. Jungnickel, V. Pohl, S. Nonnig, and C. von Helmolt, "A physical model of the wireless infrared communication channel," *IEEE J. Sel. Areas Commun.*, vol. 20, no. 3, pp. 631–640, Apr. 2002.
[32] K. V. Mardia and P. E. Jupp, *Directional Statistics*. London, U.K.: Wiley, 2000.
[33] J. Bian, C.-X. Wang, J. Huang, Y. Liu, J. Sun, M. Zhang, and E.-H.-M. Aggoune, "A 3D wideband non-stationary multi-mobility model for vehicle-to-vehicle MIMO channels," *IEEE Access*, vol. 7, pp. 32562–32577, 2019.
[34] A. Al-Kinani, C.-X. Wang, F. Haider, H. Haas, W. Zhang, and X. Cheng, "Light and RF dual connectivity for the next generation cellular systems," in *Proc. IEEE ICCC*, Qingdao, China, Oct. 2017, pp. 1–6.
[35] Transport Canberra and City Services. (Mar. 17, 2016). *Design Standards for Urban Infrastructure*. Accessed: Mar. 30, 2020. [Online]. Available: https://www.tccs.act.gov.au/
[36] Alta Planning and Design. (Jan. 2017). Urban, Rural and Suburban Complete Streets Design Manual. Cambridge, MA, USA. Accessed: Feb. 18, 2020. [Online]. Available: https://www.northamptonma.gov/DocumentCenter/View/6668
[37] Department for Transport. (Jan. 4, 2007). *Speed, Speed Limits and Stopping Distances*. Accessed: Mar. 31, 2020. [Online]. Available: http://www.brake.org.uk/rsw/15-facts-a-resources/facts/1255-speed
[38] M. Fabian, E. Lewis, T. Newe, and S. Lochmann, "Optical fibre cavity for ring-down experiments with low coupling losses," *Meas. Sci. Technol.*, vol. 21, pp. 1–5, Jul. 2010.
[39] M. L. Marceau and M. G. VanGeem. (Aug. 2008). Solar Reflectance Values of Concrete. IL, USA. Accessed: Mar. 31, 2020. [Online]. Available: http://www.cement.org
[40] Z. Ghassemlooy, L. N. Alves, S. Zvánovec, and M.-A. Khalighi, *Visible Light Communications Theory and Applications*. New York, NY, USA: CRC Press, 2017.
[41] P. Luo, Z. Ghassemlooy, H. Le Minh, E. Bentley, A. Burton, and X. Tang, "Fundamental analysis of a car to car visible light communication system," in *Proc. IEEE CSNDSP*, Manchester, U.K., Jun. 2014, pp. 1011–1016.
[42] M. Pätzold, *Mobaile Radio Channels*. Chichester, U.K.: Wiley, 2012.

AHMED AL-KINANI received the B.Sc. degree (Hons.) in laser technology and the M.Sc. degree in optical communications from the University of Technology, Baghdad, Iraq, in 2001 and 2004, respectively, and the Ph.D. degrees in optical wireless communications from the University of Edinburgh and Heriot-Watt University, Edinburgh, U.K., in 2018. He is currently a Radio Engineer with Cellular Asset Management Services. His research interests include optical wireless communications, optical channel characterization and modeling for visible light communications, and heterogeneous 5G and beyond networks. He was a recipient of the Best Paper Awards from IEEE IWCMC, in 2016.

CHENG-XIANG WANG (Fellow, IEEE) received the B.Sc. and M.Eng. degrees in communication and information systems from Shandong University, China, in 1997 and 2000, respectively, and the Ph.D. degree in wireless communications from Aalborg University, Denmark, in 2004.

He was a Research Assistant with the Hamburg University of Technology, Hamburg, Germany, from 2000 to 2001, a Visiting Researcher with Siemens AG Mobile Phones, Munich, Germany, in 2004, and a Research Fellow with the University of Agder, Grimstad, Norway, from 2001 to 2005. He has been with Heriot-Watt University, Edinburgh, U.K., since 2005, where he was promoted to a Professor, in 2011. In 2018, he joined Southeast University, China, as a Professor. He is also a part-time Professor with the Purple Mountain Laboratories, Nanjing, China. He has authored four books, two book chapters, and over 390 papers in refereed journals and conference proceedings, including 23 Highly Cited Papers. He has also delivered 20 Invited Keynote Speeches/Talks and seven Tutorials in international conferences. His current research interests include wireless channel measurements and modeling, B5G wireless communication networks, and applying artificial intelligence to wireless communication networks.

Dr. Wang is a Fellow of the IET and an IEEE Communications Society Distinguished Lecturer, in 2019 and 2020. He has served as a TPC Member, the TPC Chair, and the General Chair for more than 80 international conferences. He received eleven Best Paper Awards from IEEE GLOBECOM 2010, IEEE ICCT 2011, ITST 2012, IEEE VTC 2013-Spring, IWCMC 2015, IWCMC 2016, IEEE/CIC ICCC 2016, WPMC 2016, WOCC 2019, and IWCMC 2020. He was a Highly-Cited Researcher recognized by Clarivate Analytics, from 2017 to 2019. He has served as an Editor for nine international journals, including the IEEE Transactions on Wireless Communications, from 2007 to 2009, the IEEE Transactions on Vehicular Technology, from 2011 to 2017, and the IEEE Transactions on Communications, from 2015 to 2017. He was a Guest Editor of the IEEE Journal on Selected Areas in Communications, the Special Issue on Vehicular Communications and Networks (a Lead Guest Editor), the Special Issue on Spectrum and Energy Efficient Design of Wireless Communication Networks, and the Special Issue on Airborne Communication Networks. He was also a Guest Editor of the IEEE Transactions on Big Data, Special Issue on Wireless Big Data. He is a Guest Editor of the IEEE Transactions on Cognitive Communications and Networking, Special Issue on Intelligent Resource Management for 5G and Beyond. He is currently an Executive Editorial Committee Member of the IEEE Transactions on Wireless Communications.

QIUMING ZHU (Member, IEEE) received the B.Sc. degree in electronic engineering from the Nanjing University of Aeronautics and Astronautics (NUAA), Nanjing, China, in 2002, and the M.Sc. and Ph.D. degrees in communication and information systems, in 2005 and 2012, respectively. From 2016 to 2017, he was a Visiting Academic with Heriot-Watt University. Since 2012, he has been an Associate Professor in wireless communications. His research interests include channel modeling for 5G communication systems and wireless channel emulators.

YU FU received the B.Sc. degree in computer science from Huaqiao University, Fujian, China, in 2009, and the M.Sc. degree in information technology (mobile communications) and the Ph.D. degree in wireless communications from Heriot-Watt University, Edinburgh, U.K., in 2010 and 2015, respectively. He has been a Postdoctoral Research Associate with Heriot-Watt University, since 2015. His main research interests include advanced MIMO communication technologies, wireless channel modeling and simulation, RF tests, and software defined networks.

EL-HADI M. AGGOUNE (Life Senior Member, IEEE) received the M.S. and Ph.D. degrees in electrical engineering from the University of Washington (UW), Seattle, WA, USA. He taught graduate and undergraduate courses in electrical engineering at many universities in the USA and abroad. He served at many academic ranks, including the Endowed Chair Professor. He is listed as an Inventor in two patents assigned to the Boeing Company, USA, and the Sensor Networks and Cellular Systems Research Center, University of Tabuk, Saudi Arabia. He is also a Professional Engineer registered in WA. He is currently serving as a Professor and the Director of the SNCS Research Center, University of Tabuk. His research is referred to in many patents, including patents assigned to ABB, Switzerland, and EPRI, USA. He has authored many papers in IEEE and other journals and conferences. His research interests include wireless sensor networks, energy systems, and scientific visualization. He has been serving on many technical committees for conferences worldwide and a Reviewer for many journals. One of his Laboratories received the Boeing Supplier Excellence Award. He was a recipient of the IEEE Professor of the Year Award, UW Branch.

AHMED TALIB received the B.Sc. degree from the College of Electrical and Electronic Techniques, Baghdad, Iraq, in 2004, and the M.Sc. degree from Brunel University, London, U.K., in 2013. He is currently the Switching Department Manager with Iraqi Telecommunication and Informatics Company (ITPC), Iraq. His research interests include 5G and beyond technologies.

NIDAA A. AL-HASAANI received the B.Sc. degree in electrical engineering from Baghdad University, Iraq, in 1995, and the M.Sc. degree in electronics and communication engineering from Yildiz Technicall University, Istanbul, Turkey, in 2018. From 2005 to 2008, she was the RAN Manager with Zain Telecom, Iraq. She is currently the Chief Senior Engineer with Iraqi Telecommunication and Informatics Company (ITPC), Iraq. Her research interests include GFDM and OFDM modulations, spectrum sensing, cognitive radio, energy detection, and channel estimation.